remote sensing

MDPI

Article

A Multiple Targets ISAR Imaging Method with Removal of Micro-Motion Connection Based on Joint Constraints

Hongxu Li [1], Qinglang Guo [2], Zihan Xu [1], Xinfei Jin [1], Fulin Su [1,*] and Xiaodi Li [1]

[1] School of Electronics and Information Engineering, Harbin Institute of Technology, Harbin 150006, China; 20b905041@stu.hit.edu.cn (H.L.); 20b905051@stu.hit.edu.cn (Z.X.); 22b305004@stu.hit.edu.cn (X.L.)
[2] CETC Academy of Electronics and Information Technology Group Co., Ltd., China Academic of Electronics and Information Technology, Beijing 100070, China; gql1993@mail.ustc.edu.cn
* Correspondence: franklin_su@hit.edu.cn

Abstract: Combining multiple data sources, Digital Earth is an integrated observation platform based on air–space–ground–sea monitoring systems. Among these data sources, the Inverse Synthetic Aperture Radar (ISAR) is a crucial observation method. ISAR is typically utilized to monitor both military and civilian ships due to its all-day and all-weather superiority. However, in complex scenarios, multiple targets may exist within the same radar antenna beam, resulting in severe defocusing due to different motion conditions. Therefore, this paper proposes a multiple-target ISAR imaging method with the removal of micro-motion connections based on the integration of joint constraints. The fully motion-compensated targets exhibit low rank and local similarity in the high-resolution range profile (HRRP) domain, while the micro-motion components possess sparsity. Additionally, targets display sparsity in the image domain. Inspired by this, we formulate a novel optimization by promoting the low-rank, the Laplacian, and the sparsity constraints of targets and the sparsity constraints of the micro-motion components. This optimization problem is solved by the linearized alternative direction method with adaptive penalty (LADMAP). Furthermore, the different motions of various targets degrade their inherent characteristics. Therefore, we integrate motion compensation transformation into the optimization, accordingly achieving the separation of rigid bodies and the micro-motion components of different targets. Experiments based on simulated data demonstrate the effectiveness of the proposed method.

Keywords: Inverse Synthetic Aperture Radar (ISAR); multiple targets; Laplacian regularization; low rank; sparsity

Citation: Li, H.; Guo, Q.; Xu, Z.; Jin, X.; Su, F.; Li, X. A Multiple Targets ISAR Imaging Method with Removal of Micro-Motion Connection Based on Joint Constraints. *Remote Sens.* **2024**, *16*, 3647. https://doi.org/10.3390/rs16193647

Academic Editors: Massimiliano Pieraccini, Zhihua Zhang and M. James C. Crabbe

Received: 30 July 2024
Revised: 25 September 2024
Accepted: 26 September 2024
Published: 29 September 2024

1. Introduction

Inverse Synthetic Aperture Radar (ISAR) is widely utilized to generate high-resolution images of military or civilian targets under all-day, all-weather conditions [1–3]. The pulse-Doppler (PD) radar typically transmits linear frequency-modulated (LFM) signals with a large bandwidth to achieve high range resolution. The high azimuth resolution is obtained through the synthetic aperture formed by the relative motion between the target and the radar. Since the imaging targets are generally non-cooperative, such relative motion may introduce undesirable range migration. Therefore, many methods have been proposed in the past few decades to compensate for range migration, thereby achieving excellent performance [4,5].

However, in the modern situation (e.g., ships moving in a formation), multiple targets may appear within the same radar antenna beam, impairing the mono-target assumption. Additionally, micro-motion components are widespread among various targets. Induced by the rotating antennas or propellers, the so-called micro-Doppler effect may cause interference stripes in the imaging result, significantly degrading the image quality. Under the multi-target assumption, different targets may be connected by these interference stripes,

making it difficult to achieve focused images. Therefore, separating and imaging multiple targets under the micro-Doppler connection is a great challenge.

The existing multi-target ISAR imaging methods typically fall into three categories: time-frequency (TF)-based [6–14], segmentation-based [15–19], and parameter-based methods [20–24].

TF-based methods first extract Doppler variation along the cross-range direction. Then, different targets' TF curves are filtered in the TF domain according to the estimated variation. Based on the assumption that different targets possess their own chirp rates, Li et al. [6] first transformed the signal into the fractional Fourier transform domain. Then, the CLEAN algorithm was utilized to separate different targets. Zhang et al. [7] integrated the Radon transform with the Reassigned Smoothed Pseudo Wigner–Ville Distribution (RSPWVD), achieving significantly improved separation. Xiao et al. [10] first employed the Short-Time Fourier transform (STFT) on the overlapped echo. Then, different TF curves were filtered using a mask suitable for different chirp rates. As a result, they applied the inverse STFT on these curves to reconstruct the finally separated echoes. Nevertheless, the separation efficiency usually depends on the estimation accuracy. Moreover, many TF methods, such as Cohen's classes, suffer from a serious cross term, severely impairing their effectiveness.

Segmentation-based methods first separate different targets in the image or the high-resolution range profiles (HRRPs) domain. For the image domain, separated images are transformed back into the HRRPs domain, where motion compensation and imaging are further performed. Bai et al. [15] first simultaneously compensated for the range migration to form a "bulk" image of targets. Then, different targets were segmented through clustering methods and normalized cuts. Finally, these separated images were transformed back to the HRRPs domain to achieve the refined compensation, accordingly obtaining the well-focused targets. For the HRRPs domain, different targets are first separated in the HRRPs domain to meet the single-target assumption. Following that, the conventional imaging algorithms are then applied to the separated HRRPs. Kong et al. [16] employed the modified envelope correlation method and the Radon transform to align the HRRPs. Then, they separated different targets and further employed the Discrete chirp-Fourier transform (DCFT) to achieve final imaging. However, overlapping HRRPs and images limit the application of the segmentation-based and the HRRPs-based algorithms.

As for parameter-based methods, they typically regard the translational motion of each target as a polynomial. Then, coefficient parameters are searched through various iterative methods. Liu et al. [20] utilized the particle swarm optimization (PSO) to search coefficients, consequently compensating for the range curvature. Then, a modified CLEAN technique was applied to extract different targets. Nevertheless, the parametric methods are usually sensitive with respect to the searching step as they are all based on the parameter space.

The aforementioned methods achieve outstanding results within their specific assumptions. However, the micro-Doppler effect is not considered in their assumptions. The micro-Doppler effect, caused by micro-motion components, usually creates interference stripes along the cross-range dimension in imaging results. Over the past few decades, numerous algorithms have been developed to eliminate this interference [25,26]. Recently, micro-Doppler removal methods based on Robust Principal Component Analysis (RPCA) have received increasing attention [27]. Zhou et al. [28] utilized RPCA to decompose the target into rigid body and micro-motion components. Zhang et al. [29] extended RPCA based on the adjacent similarity among HRRPs, accordingly achieving excellent separation.

Inspired by these methods, this paper proposes a multiple-target ISAR imaging method with the removal of micro-motion connections based on the integration of joint constraints. First, micro-motion components are roughly filtered out in the image domain, and then transformed back into the HRRPs domain. Then, we apply the Radon transform to the micro-motion components to roughly estimate the target's range migration, further forming the coarse range migration transformation. Following that, we construct a constrained cost function consisting of low-rank and sparsity. The cost function is solved using the

linearized alternating direction method with adaptive penalty (LADMAP) [30] to ensure convergence, further achieving rough separation of different targets and micro-motion components. The coarse separated targets are then used to estimate a more accurate range migration transformation through a correlation-based method. Subsequently, we construct a tri-constrained cost function consisting of low-rank, sparsity, and local similarity. Finally, different targets and their micro-motion components are entirely separated. Additionally, we analyze the periodicity of the micro-motion components to ensure complete separation.

The main contributions of this paper are summarized as follows:

- We formulate a constrained optimization, consisting of the low-rank and the sparsity. Such optimization is solved by the LAMAP method to achieve the coarse separation. Consequently, the range migration is accurately estimated by a correlation-based method.
- We establish a triple-constrained problem especially for the multi-target scenario with micro-Doppler connections. Specifically, we formulate a constrained optimization, consisting of the low-rank, the sparsity, and the Laplacian constraint. Such optimization is solved by the LAMAP method to achieve complete separation.
- We modified the mono-target assumption and extended it to a multi-target scenario with micro-Doppler connections. Under this framework, the micro-Doppler effect is eliminated, and the targets are separated. In the proposed framework, different norms correspond to different signal characteristics, which effectively demonstrates the applicability of our approach.

The remainder of this article is organized as follows: Section 2 models the signal model of multiple targets under the micro-Doppler scenarios. Section 3 analyzes the signal characteristics. Section 4 gives a detailed description of the proposed procedure. Section 5 evaluates the performances of the proposed method through the simulated data. Finally, the conclusions are given in Section 6.

2. Imaging Model

In this section, we will briefly introduce the multi-target ISAR signal model with micro-Doppler connections.

The imaging geometry model of multiple targets is presented in Figure 1. The PD radar is located at the origin point O of the XOY coordinate system. Blue lines represent the radar antenna beam. Moving in various directions, different targets exist within the same antenna beam, resulting in multiple range migrations along the line of sight (LOS) of the radar. Collectively referred to as translational motion, these range migrations may result in severe defocusing in imaging results. Additionally, the target's orientation rotates by a certain angle around its rotational center during the imaging interval. This rotation generates a synthetic aperture, leading to high resolution along the cross-range dimension of the imaging results.

In ISAR imaging, a target is generally regarded as a cluster of scatterers. Therefore, the signal reflected from a target is considered as the summation of the signals reflected by each scatterer. The PD radar transmits linear frequency-modulated (LFM) signals with a large bandwidth. Hence, the signal received by the radar receiver can be written as

$$S_1(t_r, t_m) = \sum_{i=1}^{Z} I_i \mathrm{rect}\left(\frac{t_r - 2R_i(t_m)/c}{T_P}\right) \exp\left(j2\pi f_c\left(t_r - \frac{2R_i(t_m)}{c}\right)\right) \exp\left(j\pi\gamma\left(t_r - \frac{2R_i(t_m)}{c}\right)^2\right) \quad (1)$$

where t_r and t_m represent the fast time and the slow time, respectively. Z denotes the total number of scatterers. I_i represents the amplitude of the i-th scatterer. f_c, γ , and T_p represent the basic frequency, the chirp rate, and the pulse width of the signal, respectively. R_i denotes the instantaneous distance between the i-th scatterer and the radar. Typically,

dechirp processing is employed on the reflected signal to reduce the bandwidth. Therefore, the echo after dechirp processing can be derived as

$$S_2(t_r, t_m) = \sum_{i=1}^{Z} I_i \text{rect}\left(\frac{t_r - 2R_i(t_m)/c}{T_P}\right) \exp\left(-j\frac{4\pi\gamma}{c}\left(t_r - \frac{2R_{\text{ref}}}{c}\right)\Delta R_i(t_m)\right) \exp\left(-j\frac{4\pi f_c}{c}\Delta R_i(t_m)\right) \exp\left(j\frac{4\pi\gamma}{c^2}\Delta R_i^2(t_m)\right) \tag{2}$$

where R_{ref} denotes the reference range of the dechirp signal. ΔR_i is the difference between the instantaneous distance and the reference range of the i-th scatterer. ΔR_i is written as R_i in the following formula as different scatterers share the same reference range. Applying the fast Fourier transform along the t_r direction to the (2), the HRRPs are written as

$$S_3(f_r, t_m) = \sum_{i=1}^{Z} I_i \text{sinc}\left[T_P\left(f_r + 2\frac{\gamma}{c}R_i(t_m)\right)\right] \cdot \exp\left(-j\frac{4\pi f_c}{c}R_i(t_m)\right) \tag{3}$$

where f_r represents the range frequency of the target. As previously mentioned, the motion of a target consists of the translational motion and the rotational motion. The overall motion R_i and its translational and rotational components are written as

$$R_i(t_m) = R_s(t_m) + R_l(t_m) \tag{4}$$

$$R_s(t_m) = x_i \sin(\theta(t_m)) + y_i \cos(\theta(t_m)) \tag{5}$$

$$R_l(t_m) = R_0 + vt_m + \frac{1}{2}at_m^2 + \ldots + \frac{1}{n!}a_n t_m^n \tag{6}$$

where R_s and R_l represent the rotational motion and the translational motion, respectively. x_i and y_i denote the abscissa and the ordinate of the i-th scatterer in the target coordinate. θ_m is the rotational angle of the target. R_0 represents the initial distance between the target center and the radar. v, a, and a_n represent the target's velocity, acceleration, and n-th order acceleration, respectively. For most non-cooperative targets, the imaging interval is relatively short, leading to small rotation angles. Therefore, we obtain

$$R_s(t_m) = x_i\theta(t_m) + y_i \tag{7}$$

$$R_l(t_m) = R_0 + vt_m + \frac{1}{2}at_m^2 \tag{8}$$

The rotational motion represented by (7) leads to high resolution along the cross-range dimension, while the translational motion represented by (8) results in severe defocusing. In addition, this paper focuses on the separation of multiple targets with different motion characteristics within a smaller range. Under the multi-target assumption, R_l belongs to its own coordinate systems. Therefore, conventional range alignment methods fail to achieve unified motion compensation for multiple targets.

In addition to rigid body parts, most non-cooperative targets contain micro-motion components that rotate at high speeds (e.g., engines in aircraft, propellers, and antennas on ships). The motion of these micro-motion components is usually superimposed on the rotation of the rigid body. The Doppler shifts caused by the micro-motion components are also superimposed on the echoes of the rigid body. This Doppler shift induced by micro-motion components is known as the micro-Doppler effect. As illustrated in Figure 2, we place the rotational center of the target's rigid body at the origin of the XOY coordinate system. The rotational center of the micro-motion components is set at the origin of the $X'O'Y'$ coordinate system, which serves as the motion coordinate system for the micro-motion components themselves. Additionally, the origin of the $X'O'Y'$ coordinate system is set on the rigid body scatterer, meaning that this coordinate system rotates along with the rigid body.

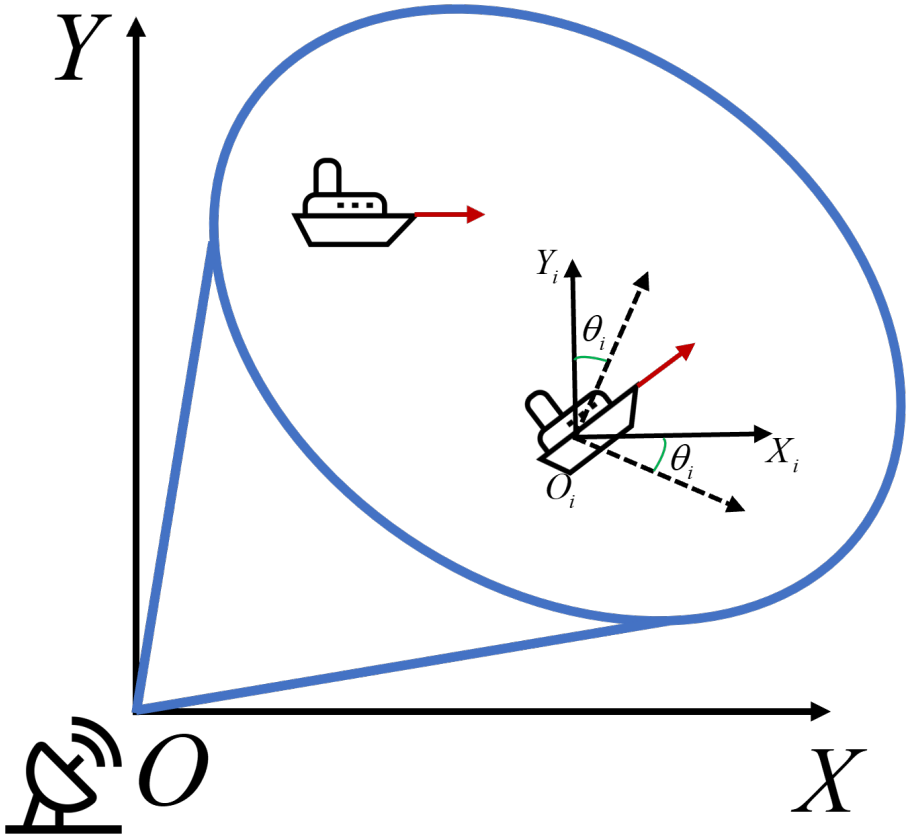

Figure 1. The imaging geometry of multiple targets.

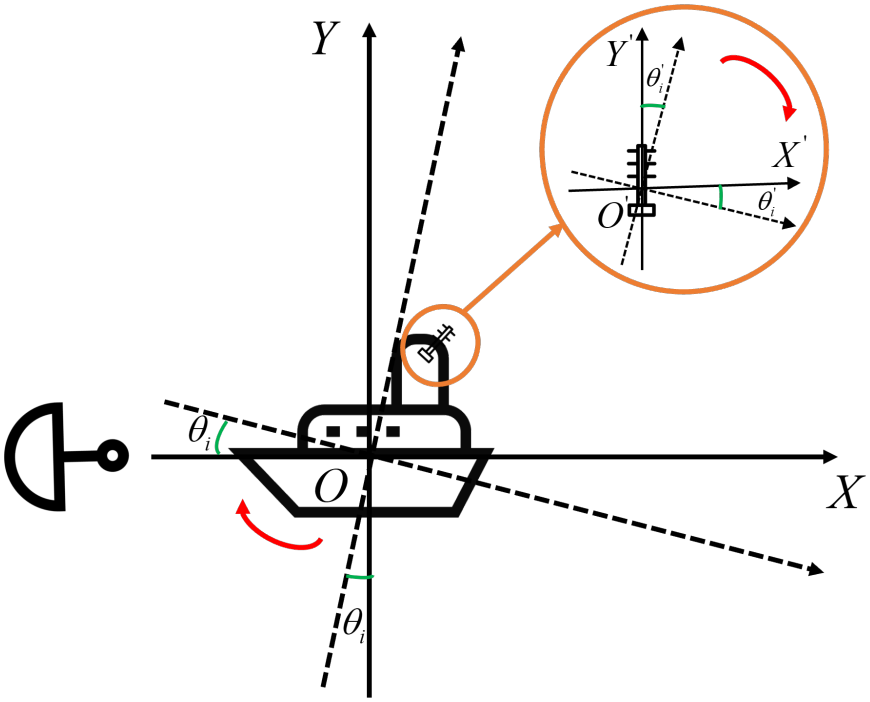

Figure 2. The imaging geometry of the micro-motion components.

Suppose that the scatterer $K(x_k, y_k)$ on the rotating antenna rotates around its own rotational center with a rotational angle of θ' and a rotational shaft of r_k. The initial angle of the micro-motion components is θ_k. The instantaneous distance between the scatterer and the radar is given as

$$R_K(t_m) = x_K \sin(\theta(t_m)) + y_K \cos(\theta(t_m)) + r_K \cos\left(\theta^{'}(t_m) + \theta_k\right) \tag{9}$$

According to the aforementioned approximation, we obtain

$$R_K(t_m) = x_K \theta(t_m) + y_K + r_K \cos\left(\theta^{'}(t_m) + \theta_k\right) \tag{10}$$

It is seen that the cosine term exhibits multiple periods within the imaging interval as the variation of $\theta^{'}$ is much greater than that of θ. These periods result in interference stripes in the imaging results. In the next section, we will describe the procedure of simultaneously separating targets and micro-Doppler interferences in detail.

3. Analysis of the Signal Characteristics

In this section, we will analyze the unique characteristics of the micro-motion components and the rigid body signal. First, the low-rank property of the rigid body in the HRRPs domain is theoretically determined by the number of the scattering points. Assuming that the translational motion of the target has been fully compensated, performing a fast Fourier transform (FFT) on a single scatterer in (3) along the f_r direction yields

$$s(t_r, t_m) = I \exp(-j\frac{4\pi(\gamma t_r + f_c)}{c}(x\theta(t_m) + y)) \tag{11}$$

which can be discretized as

$$s(n, p) = I \exp\left(-j\frac{4\pi\gamma\Delta t_r}{c} yn\right) \cdot \exp\left(-j\frac{4\pi f_c \Delta\theta}{c} xp\right) \tag{12}$$

where n and p are the index of the range cell and the pulse, respectively. Suppose that the size of the HRRP matrix is N $\times$ P, (12) can be written as

$$s(n, p) = I\mathbf{a}^T\mathbf{b} \tag{13}$$

where $\mathbf{a} = [a_1, \ldots, a_N]$ and $\mathbf{b} = [b_1, \ldots, b_P]$ with $a_i = \exp(-j4\pi\gamma yi\Delta t_r/c)$ and $b_i = \exp(-j4\pi f_c xi\Delta t_r/c)$, respectively. For a target composed of U scattering points, its echo can be expressed as

$$s(n, p) = \sum_{u}^{\mathrm{U}} I_u \mathbf{a}_u^T \mathbf{b}_u \tag{14}$$

Based on the properties of rank, the maximum rank of this HRRP matrix does not exceed U. Thus, an echo with well-compensated motion can be considered low rank. However, undesirable motion disrupts this characteristic. Therefore, we leverage the inherent low-rank nature of the echo to separate targets with different motions.

For the sparsity of rigid body signals in the image domain and micro-motion components in the HRRPs domain, the sparsity of a rigid body signal in the image domain is theoretically determined by the number of scatterers. In contrast, micro-motion components typically occupy several range cells and form stripes across the entire Doppler domain in the image domain, resulting in lower sparsity. Conversely, the signal of the micro-motion components in the HRRPs domain occupies only a few range cells, demonstrating strong sparsity.

We conducted an experiment to verify such characteristics. Figure 3 shows the range profiles and the imaging results of the rigid body and the micro-motion components. Figure 3a,b present the range profiles and the imaging results of the ridge body, while Figure 3c,d show those for the micro-motion components. In the HRRPs domain, the rate of non-zero pixels for the rigid body and micro-motion components is 0.22 and 0.02, respectively, confirming the sparsity of the micro-motion components in the HRRPs domain. Moreover, the absolute value of the rate of non-zero pixels may be dependent on the selected range after pulse compression, while the relative value depends on the size ratio between

the rigid body and the micro-motion components. Therefore, micro-motion components exhibit a much stronger sparsity in the HRRPs domain compared to the rigid body. In the image domain, the rate of non-zero pixels for the rigid body and the micro-motion components is 0.01 and 0.06, respectively, verifying the sparsity of the rigid body in the image domain.

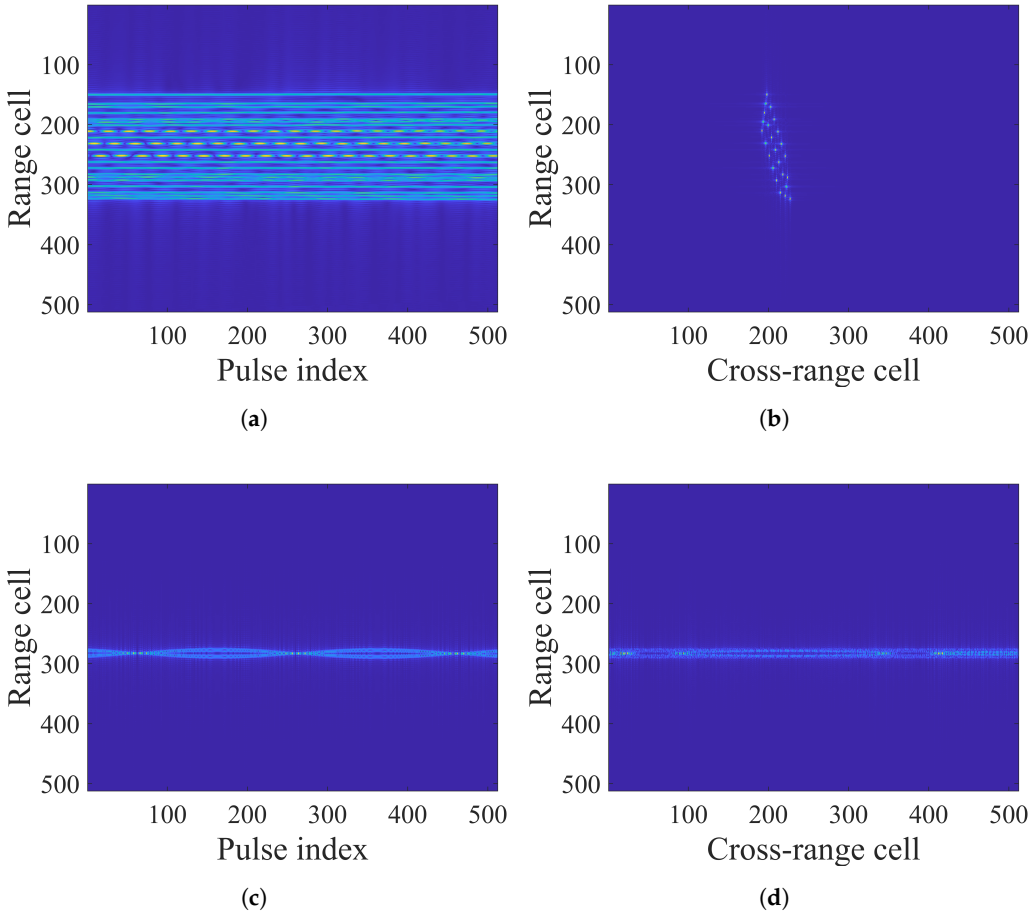

Figure 3. Range profiles and the imaging results of the ridge body and the micro-motion components. (**a**) Range profiles of the ridge body. (**b**) Imaging result of the ridge body. (**c**) Range profiles of the micro-motion components. (**d**) Imaging result of the micro-motion components.

Additionally, rigid body signals exhibit strong similarity in adjacent pulses, with this similarity weakening as the distance increases. In contrast, micro-motion components do not possess this local similarity. Figure 4 presents the autocorrelation of the rigid body and micro-motion components in the HRRP domain. Figure 4a,c show the correlation coefficients for the rigid body and micro-motion components, respectively. To present this more clearly, we extracted the correlation coefficients of the 256th pulse and illustrated them in Figure 4b,d. It can be observed that the HRRP matrix of the rigid body exhibits strong similarity in a few adjacent pulses, with the similarity diminishing as the pulses get farther apart. The HRRP matrix of the micro-motion components does not show this property, further validating the local similarity of the rigid body in the HRRP domain. In the next section, we will utilize these properties to construct our framework about the multiple targets separation with removal of the micro-motion connection.

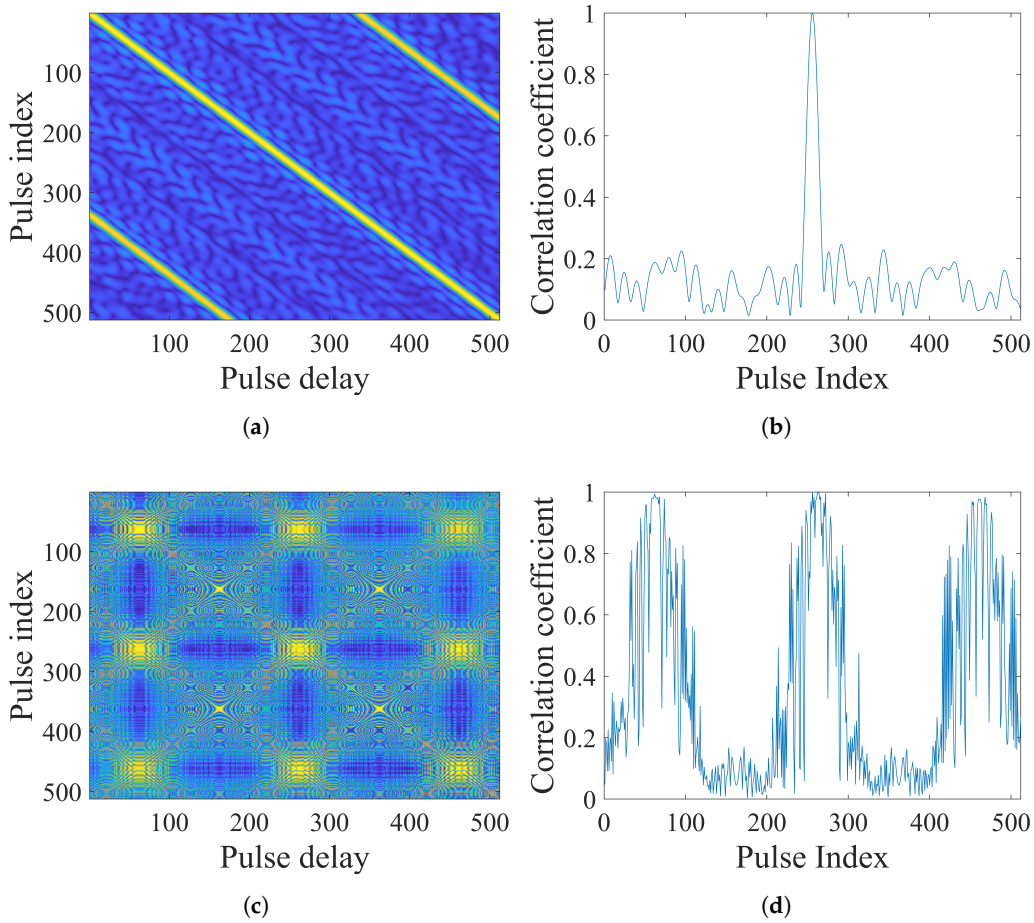

Figure 4. Range profiles and the imaging results of the ridge body and the micro-motion components. (**a**) Correlation coefficients of the ridge body. (**b**) Correlation coefficients of 256th pulse of the ridge body. (**c**) Correlation coefficients of the micro-motion components. (**d**) Correlation coefficients of 256th pulse of the micro-motion components.

4. Multiple Targets Separation Method with Removal of Micro-Motion Connection Based on Dual Optimization

In this section, we will explain our proposed multiple targets method with removal of micro-motion connection based on dual optimization in detail. First, we roughly filter out the micro-motion components in the image domain and transform them back to the HRRPs domain. Then, we estimate the motion parameters of these filtered micro-motion components using the Radon transform. These parameters are then utilized to construct a coarse motion compensation function. Following that, we integrate the coarse range migration transformation with the dual-constrained optimization model to form a cost function. This cost function is solved by utilizing LADMAP to coarsely separate targets and micro-motion components. Subsequently, we employ a correlation-based range alignment algorithm to measure the motion parameters of the coarsely separated targets. These parameters are utilized to construct a more precious range migration transformation. This more accurate range migration transformation is then incorporated into a triple-constrained optimization model. Similarly, this cost function is solved using LADMAP to ensure convergence. Finally, different targets and micro-motion components are completely separated. Figure 5 illustrates the detailed procedure of our proposed algorithm. We will elaborate on each step of this process in the following subsections.

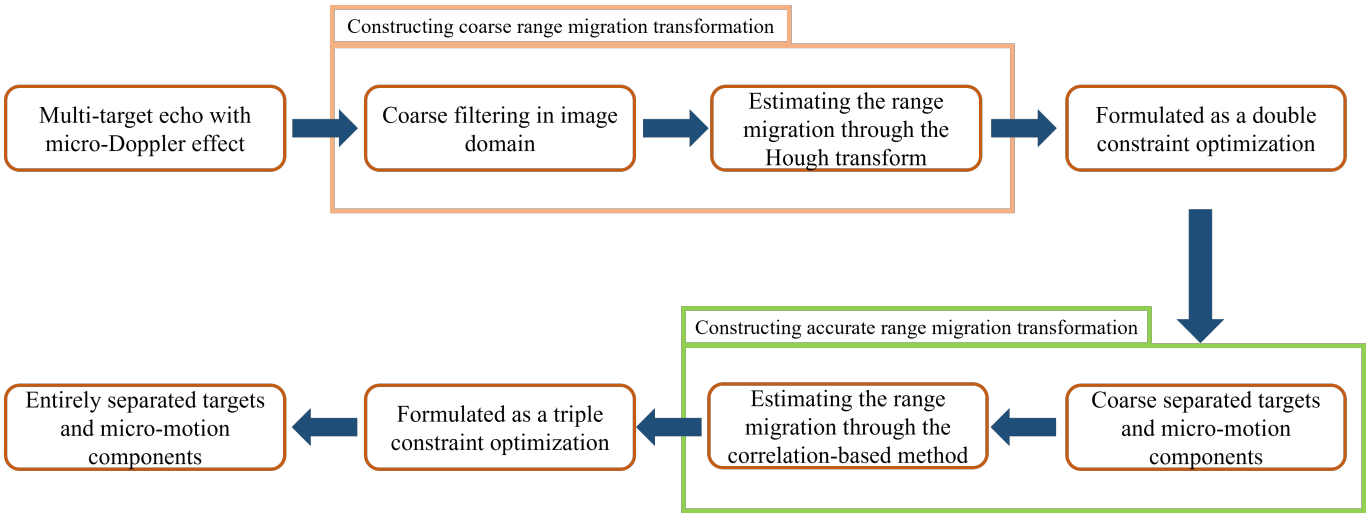

Figure 5. The procedure of the proposed multi-target separation method.

4.1. Constructing Coarse Range Migration Transformation

First, we transform the multi-target echo with micro-Doppler effects into the image domain and use a constant threshold to roughly filter out the micro-motion components. Then, the micro-motion components are transformed back into the HRRPs domain. Since the micro-motion components and the targets share the same motion, the Radon transform is allowed to roughly extract the motion parameters of the targets. Based on these motion parameters, a coarse range migration transformation is constructed.

4.2. Coarse Separating through Double-Constraint Optimization

Motion-compensated targets exhibit low-rank characteristics in the HRRPs domain and sparsity in the image domain. Micro-Doppler components also exhibit sparsity as they occupy fewer range cells. Since the rotational speed of the micro-motion components is generally much higher than that of the rigid body, the low-rank characteristics of the micro-motion components in the HRRPs domain are weaker than those of the rigid body. Based on these inherent properties, we construct a dual-constrained cost function as follows:

$$\begin{aligned} &\sum_{d=1}^{D} \operatorname{rank}(\mathbf{L}_d) + \sum_{d=1}^{D} \|\mathbf{S}_d\|_0 + \|\mathbf{S}_{MD}\|_0 \\ &\text{s.t. } \mathbf{H} = \sum_{d=1}^{D} R_d(\mathbf{L}_d) + \mathbf{S}_{MD} \\ &\mathbf{L}_d = \mathrm{IFFT}(\mathbf{S}_d) \end{aligned} \tag{15}$$

where $\mathbf{L}_d$ and $\mathbf{S}_d$ denote the rigid body in the HRRPs domain and in the image domain with the target index of d. $\mathbf{S}_{MD}$ represents the micro-motion components in the HRRPs domain. $\mathbf{H}$ denotes the original multi-target echo with micro-Doppler effects. R_d is the range migration transformation of the d-th target. Since (15) is a non-convex problem, $\operatorname{rank}(\mathbf{L}_d)$ and $\|\mathbf{S}_d\|_0$ are generally relaxed to $\|\mathbf{L}_d\|_*$ and $\|\mathbf{S}_d\|_1$. This leads to

$$\begin{aligned} &\sum_{d=1}^{D} \|\mathbf{L}_d\|_* + \sum_{d=1}^{D} \|\mathbf{S}_d\|_1 + \|\mathbf{S}_{MD}\|_1 \\ &\text{s.t. } \mathbf{H} = \sum_{d=1}^{D} R_d(\mathbf{L}_d) + \mathbf{S}_{MD} \\ &\mathbf{L}_d = \mathrm{IFFT}(\mathbf{S}_d) \end{aligned} \tag{16}$$

whose augmented Lagrange function is accordingly written as

$$\begin{aligned}\mathcal{L}(\mathbf{L}_d, \mathbf{S}_d, \mathbf{S}_{MD}, \mathbf{Y}_d, \mathbf{Y}_E) = &\sum_{d=1}^{D} \|\mathbf{L}_d\|_* + \sum_{d=1}^{D} \|\mathbf{S}_d\|_1 + \|\mathbf{S}_{MD}\|_1 \\ &+ \sum_{d=1}^{D} \langle \mathbf{Y}_d, \mathbf{L}_d - \mathrm{IFFT}(\mathbf{S}_d) \rangle + \sum_{d=1}^{D} \frac{\mu_d}{2} \|\mathbf{L}_d - \mathrm{IFFT}(\mathbf{S}_d)\|_F^2 \\ &+ \langle \mathbf{Y}_E, \mathbf{H} - R_1(\mathbf{L}_1) - R_2(\mathbf{L}_2) - \mathbf{S}_{MD} \rangle \\ &+ \frac{\mu_E}{2} \|\mathbf{H} - R_1(\mathbf{L}_1) - R_2(\mathbf{L}_2) - \mathbf{S}_{MD}\|_F^2\end{aligned} \tag{17}$$

where $\|\cdot\|_*$, $\|\cdot\|_1$, and $\|\cdot\|_F$ denote the nuclear norm, l_1-norm, and Frobenius norm, respectively. $<\cdot>$ denotes the inner product operator. $\mathbf{Y_d}$ and $\mathbf{Y_E}$ represent the Lagrange multiplier matrices of the d-th target and the overall summation equation, respectively. Suppose that two targets emerge in the same radar antenna beam (i.e., $D = 2$), the augmented Lagrange function is decomposed by the LADMAP into the following sub-problems as

$$\begin{cases} \mathbf{L}_d^{(k+1)} = \min\limits_{\mathbf{L}_d} \mathcal{L}\left(\mathbf{L}_1, \mathbf{L}_2, \mathbf{Y}^{(k)}\right) \\ \mathbf{S}_d^{(k+1)} = \min\limits_{\mathbf{S}_d} \mathcal{L}\left(\mathbf{S}_1, \mathbf{S}_2, \mathbf{Y}^{(k)}\right) \\ \mathbf{S}_{MD}^{(k+1)} = \min\limits_{\mathbf{S}_{MD}} \mathcal{L}\left(\mathbf{L}_1, \mathbf{L}_2, \mathbf{Y}^{(k)}\right) \\ \mathbf{Y}_1^{(k+1)} = \mathbf{Y}_1^{(k)} + \mu_1\left(\mathbf{L}_1^{(k)} - \mathrm{IFFT}(\mathbf{S}_1)\right) \\ \mathbf{Y}_2^{(k+1)} = \mathbf{Y}_2^{(k)} + \mu_2\left(\mathbf{L}_2^{(k)} - \mathrm{IFFT}(\mathbf{S}_2)\right) \\ \mathbf{Y}_E^{(k+1)} = \mathbf{Y}_E^{(k)} + \mu_E(\mathbf{H} - R_1(\mathbf{L}_1) - R_2(\mathbf{L}_2) - \mathbf{S}_{MD}) \end{cases} \tag{18}$$

where k denotes the iteration index. Through alternately solving the sub-problems in (18), we make (17) solvable. Furthermore, the LADMAP algorithm decomposes and linearizes the complex optimization problem into subproblems, ensuring the convergence of the solution process. To update $\mathbf{L}_1$, we fix all variables except $\mathbf{L}_1$, and subsequently derive the augmented Lagrange function as

$$\begin{aligned}\mathcal{L}(\mathbf{L}_1) = &\|\mathbf{L}_1\|_* + \langle \mathbf{Y}_1, \mathbf{L}_1 - \mathrm{IFFT}(\mathbf{S}_1) \rangle + \frac{\mu_1}{2} \|\mathbf{L}_1 - \mathrm{IFFT}(\mathbf{S}_1)\|_F^2 \\ &+ \langle \mathbf{Y}_H, \mathbf{H} - R_1(\mathbf{L}_1) - R_2(\mathbf{L}_2) - \mathbf{S}_{MD} \rangle + \frac{\mu_E}{2} \|\mathbf{H} - R_1(\mathbf{L}_1) - R_2(\mathbf{L}_2) - \mathbf{S}_{MD}\|_F^2\end{aligned} \tag{19}$$

Based on the LAMDAP, we approximate (19) at $\mathbf{L}_1 = \mathbf{L}_1^{(k)}$ as

$$\begin{aligned}\mathcal{L}(\mathbf{L}_1) &\approx \|\mathbf{L}_1\|_* + \left\langle \nabla_{\mathbf{L}_1} q\left(\mathbf{L}_1^{(k)}\right), \mathbf{L}_1 - \mathbf{L}_1^{(k)} \right\rangle + \frac{\eta}{2} \left\|\mathbf{L}_1 - \mathbf{L}_1^{(k)}\right\|_F^2 \\ &= \|\mathbf{L}_1\|_* + \frac{\eta}{2} \left\|\mathbf{L}_1 - \mathbf{L}_1^{(k)} + \nabla_{\mathbf{L}_1} q\left(\mathbf{L}_1^{(k)}\right)/\eta\right\|_F^2\end{aligned} \tag{20}$$

where $\nabla_{\mathbf{L}_1} q\left(\mathbf{L}_1^{(k)}\right)$ is written as

$$\nabla q(\mathbf{L}_1) = \mathbf{Y}_1 + \mu_1(\mathbf{L}_1 - \mathrm{IFFT}(\mathbf{S}_1)) - R_1^*(\mathbf{Y}_E) - \mu_E R_1^*(\mathbf{H} - R_1(\mathbf{L}_1) - R_2(\mathbf{L}_2) - \mathbf{S}_{MD}) \tag{21}$$

Utilizing the singular value shrinkage threshold (SVT) operator, the function has a closed-form solution as

$$\mathbf{L}_1^{(k+1)} = \Re_{1/\eta}\left(\mathbf{L}_1^k - 1/\eta \nabla q(\mathbf{L}_1)\right) \tag{22}$$

where $\Re_y(\mathbf{x})$ denote shrinking the singular matrix of x utilizing the soft threshold y [31]. This operator can be specifically written as

$$\Re_y(\mathbf{x}) = \mathbf{U}\big(\zeta_y(\sigma)\big)\mathbf{V}^H \tag{23}$$

where σ denote the singular matrix, i.e., $\mathbf{x} = \mathbf{U}\sigma\mathbf{V}^H$. $\mathbf{U}$ and $\mathbf{V}$ denote the unitary matrix about $\mathbf{x}$. $\zeta_y(\sigma)$ denotes the soft threshold operator, which can be written as

$$\zeta_y(\sigma) = \mathrm{sgn}(\sigma) * \max(|\sigma| - y, 0) \tag{24}$$

Since the process of updating $\mathbf{L}_1$ is the same as $\mathbf{L}_2$, we omit it here and derive the augmented Lagrange function of $\mathbf{S}_1$ as

$$\mathcal{L}(\mathbf{S}_1) = \|\mathbf{S}_1\|_1 + \langle \mathbf{Y}_1, \mathbf{L}_1 - \mathrm{IFFT}(\mathbf{S}_1)\rangle + \frac{\mu_1}{2}\|\mathbf{L}_1 - \mathrm{IFFT}(\mathbf{S}_1)\|_F^2 \tag{25}$$

Similarly, the gradient of a part of (25) is written as

$$\nabla q(\mathbf{S}_1) = -\mathrm{FFT}(\mathbf{Y}_1) - \mu_1 \mathrm{FFT}(\mathbf{L}_1 - \mathrm{IFFT}(\mathbf{S}_1)) \tag{26}$$

which leads (25) to be approximated as

$$\begin{aligned} \mathcal{L}(\mathbf{S}_1) &\approx \|\mathbf{S}_1\|_* + \left\langle \nabla_{\mathbf{S}_1} q\left(\mathbf{S}_1^{(k)}\right), \mathbf{S}_1 - \mathbf{S}_1^{(k)} \right\rangle + \frac{\eta}{2}\left\|\mathbf{S}_1 - \mathbf{S}_1^{(k)}\right\|_F^2 \\ &= \|\mathbf{S}_1\|_* + \frac{\eta}{2}\left\|\mathbf{S}_1 - \mathbf{S}_1^{(k)} + \nabla_{\mathbf{S}_1} q\left(\mathbf{S}_1^{(k)}\right)/\eta\right\|_F^2 \end{aligned} \tag{27}$$

Utilizing (24), the close-form solution of (27) is given as

$$\mathbf{S}_1^{(k+1)} = \Im_{1/\eta}\left(\mathbf{S}_1^k - 1/\eta \nabla q(\mathbf{S}_1)\right) \tag{28}$$

As previously mentioned, we omit the processing of $\mathbf{S}_1$.

As for the range profiles of the micro-motion components $\mathbf{S}_{MD}$, the augmented Lagrange function is written as

$$\begin{aligned} \mathcal{L}(\mathbf{S}_{MD}) = \|\mathbf{S}_{MD}\|_1 &+ \langle \mathbf{Y}_E, \mathbf{H} - R_1(\mathbf{L}_1) - R_2(\mathbf{L}_2) - \mathbf{S}_{MD}\rangle \\ &+ \frac{\mu_E}{2}\|\mathbf{H} - R_1(\mathbf{L}_1) - R_2(\mathbf{L}_2) - \mathbf{S}_{MD}\|_F^2 \end{aligned} \tag{29}$$

The gradient is also derived as

$$\nabla q(\mathbf{S}_{MD}) = -\mathbf{Y}_E - \mu_E(\mathbf{H} - R_1(\mathbf{L}_1) - R_2(\mathbf{L}_2) - \mathbf{S}_{MD}) \tag{30}$$

The close-form solution is derived as

$$\mathbf{S}_{MD}^{(k+1)} = \Im_{1/\eta}\left(\mathbf{S}_{MD}^k - 1/\eta \nabla q(\mathbf{S}_{MD})\right) \tag{31}$$

Finally, the Lagrange multipliers $\mathbf{Y}_1$, $\mathbf{Y}_2$, and $\mathbf{Y}_E$ are updated as

$$\mathbf{Y}_1^{(k+1)} = \mathbf{Y}_1^k + \mu_1(\mathbf{L}_1 - \mathrm{IFFT}(\mathbf{S}_1)) \tag{32}$$

$$\mathbf{Y}_2^{(k+1)} = \mathbf{Y}_2^k + \mu_2(\mathbf{L}_2 - \mathrm{IFFT}(\mathbf{S}_2)) \tag{33}$$

$$\mathbf{Y}_E^{(k+1)} = \mathbf{Y}_E^k + \mu_E(\mathbf{H} - R_1(\mathbf{L}_1) - R_2(\mathbf{L}_2) - \mathbf{S}_{MD}) \tag{34}$$

To illustrate more clearly, such a separation model is summarized in Algorithm 1. ε is set as 1.05 to accelerate the convergence. Additionally, the employed LADMAP algorithm iteratively refines the Lagrange multipliers and adaptively adjusts during computation.

Therefore, we initialize the Lagrange multiplier matrix $\mathbf{Y}_1$, $\mathbf{Y}_2$, and $\mathbf{Y}_E$ as the zero matrix in Algorithm 1.

Algorithm 1 Double-constraint-based coarse separation

Input: Range profiles $\mathbf{H}$, Coarse motion compensation transformation of target1 $R_1(\cdot)$, Coarse motion compensation transformation of target2 $R_2(\cdot)$.

Output: HRRPs of target1 $\mathbf{L}_1$, HRRPs of target2 $\mathbf{L}_2$, HRRPs of micro-motion components $\mathbf{S}_{MD}$, Imaging result of target1 $\mathbf{S}_1$, Imaging result of target2 $\mathbf{S}_2$.

Initialization: $\mathbf{L}_1^{(0)} = \mathbf{L}_2^{(0)} = \mathbf{S}_1^{(0)} = \mathbf{S}_2^{(0)} = \mathbf{S}_1^{(0)} = \mathbf{Y}_E^{(0)} = \mathbf{Y}_1^{(0)} = \mathbf{Y}_2^{(0)} = \mathbf{0}^{N\times M}$, $\mu_1 = \mu_2 = \mu_E = 10^{-4}$, $\varepsilon = 1.05$.

while not converged **do**

The update of the rigid body in the HRRPs domain.

$$\nabla q(\mathbf{L}_1) = \mathbf{Y}_1 + \mu_1(\mathbf{L}_1 - \mathrm{IFFT}(\mathbf{S}_1)) - R_1^*(\mathbf{Y}_E) \\ -\mu_E R_1^*(\mathbf{H} - R_1(\mathbf{L}_1) - R_2(\mathbf{L}_2) - \mathbf{S}_{MD})$$

$$\mathbf{L}_1^{(k+1)} = \Re_{1/\eta}\left(\mathbf{L}_1^k - 1/\eta\nabla q(\mathbf{L}_1)\right)$$

$$\nabla q(\mathbf{L}_2) = \mathbf{Y}_2 + \mu_2(\mathbf{L}_2 - \mathrm{IFFT}(\mathbf{S}_2)) - R_2^*(\mathbf{Y}_E) \\ -\mu_E R_2^*(\mathbf{H} - R_1(\mathbf{L}_1) - R_2(\mathbf{L}_2) - \mathbf{S}_{MD})$$

$$\mathbf{L}_2^{(k+1)} = \Re_{1/\eta}\left(\mathbf{L}_2^k - 1/\eta\nabla q(\mathbf{L}_2)\right)$$

The update of the rigid body in the image domain.

$$\nabla q(\mathbf{S}_1) = -\mathrm{FFT}(\mathbf{Y}_1) - \mu_1\mathrm{FFT}(\mathbf{L}_1 - \mathrm{IFFT}(\mathbf{S}_1))$$

$$\mathbf{S}_1^{(k+1)} = \Im_{1/\eta}\left(\mathbf{S}_1^k - 1/\eta\nabla q(\mathbf{S}_1)\right)$$

$$\nabla q(\mathbf{S}_2) = -\mathrm{FFT}(\mathbf{Y}_2) - \mu_2\mathrm{FFT}(\mathbf{L}_2 - \mathrm{IFFT}(\mathbf{S}_2))$$

$$\mathbf{S}_2^{(k+1)} = \Im_{1/\eta}\left(\mathbf{S}_2^k - 1/\eta\nabla q(\mathbf{S}_2)\right)$$

The update of the micro-motion components in the HRRPs domain.

$$\nabla q(\mathbf{S}_{MD}) = -\mathbf{Y}_E - \mu_E(\mathbf{H} - R_1(\mathbf{L}_1) - R_2(\mathbf{L}_2) - \mathbf{S}_{MD})$$

$$\mathbf{S}_{MD}^{(k+1)} = \Im_{1/\eta}\left(\mathbf{S}_{MD}^k - 1/\eta\nabla q(\mathbf{S}_{MD})\right)$$

The update of the the Lagrange multiplier matrices.

$$\mathbf{Y}_1^{(k+1)} = \mathbf{Y}_1^k + \mu_1(\mathbf{L}_1 - \mathrm{IFFT}(\mathbf{S}_1))$$

$$\mathbf{Y}_2^{(k+1)} = \mathbf{Y}_2^k + \mu_1(\mathbf{L}_2 - \mathrm{IFFT}(\mathbf{S}_2))$$

$$\mathbf{Y}_E^{(k+1)} = \mathbf{Y}_E^k + \mu_E(\mathbf{H} - R_1(\mathbf{L}_1) - R_2(\mathbf{L}_2) - \mathbf{S}_{MD})$$

$\mu_1 = \varepsilon\mu_1$, $\mu_2 = \varepsilon\mu_2$,$\mu_E = \varepsilon\mu_E$

$k = k + 1$;

end while

4.3. Constructing Accurate Range Migration Transformation

By solving the coarse cost function, different targets and micro-motion components are preliminarily separated. Consequently, we employ a correlation-based range alignment method to estimate the range migration of different targets. Specifically, we use the maximum-correlation range alignment (MCRA) algorithm to estimate the precise range migration of different targets. These parameters are then used to generate more accurate r range migration transformation.

4.4. Accurate Separating through Triple-Constraint Optimization

As previously mentioned, micro-motion components exhibit high rotational speeds, significantly reducing their similarity between adjacent pulses. Typically, rigid bodies have lower rotational speeds, with a rotation angle of 2 degrees within the imaging interval. This characteristic motivates us to incorporate local similarity into the multi-target optimization. Specifically, we integrate Laplacian regularization into the cost function, forming a triple-constrained cost function as follows:

$$\begin{aligned} &\sum_{d=1}^{D}\left(\operatorname{rank}(\mathbf{L}_d)+\beta_1\operatorname{Tr}\left(\mathbf{L}_d\mathbf{B}\mathbf{L}_d^H\right)+\|\mathbf{S}_d\|_0\right)+\|\mathbf{S}_{MD}\|_0 \\ &\text{s.t. } \mathbf{H}=\sum_{d=1}^{D}R_d(\mathbf{L}_d)+\mathbf{S}_{MD} \\ &\quad\mathbf{L}_d=\operatorname{IFFT}(\mathbf{S}_d) \end{aligned} \tag{35}$$

where β denotes the penalty parameter of the Laplacian regularization. $\mathbf{B}$ denotes the graph Laplacian matrix [32], which is given as

$$\mathbf{B}=\mathbf{D}-\mathbf{W} \tag{36}$$

where $\mathbf{D}$ and $\mathbf{W}$ represent the degree matrix and the weight matrix, respectively. These two matrices are further given as

$$\mathbf{D}_{ii}=\sum_j W_{ij} \tag{37}$$

$$W_{ij}=\begin{cases} 1 & i=j \\ a & |i-j|<b \\ 0 & \text{otherwise} \end{cases} \tag{38}$$

where a and b are set as 0.8 and 3. Additionally, the cost function is similarly relaxed as

$$\begin{aligned} &\sum_{d=1}^{D}\left(\operatorname{rank}(\mathbf{L}_d)+\beta_1\operatorname{Tr}\left(\mathbf{L}_d\mathbf{B}\mathbf{L}_d^H\right)+\|\mathbf{S}_d\|_0\right)+\|\mathbf{S}_{MD}\|_1 \\ &\text{s.t. } \mathbf{H}=\sum_{d=1}^{D}R_d(\mathbf{L}_d)+\mathbf{S}_{MD} \\ &\quad\mathbf{L}_d=\operatorname{IFFT}(\mathbf{S}_d) \end{aligned} \tag{39}$$

Utilizing the LADMAP, we derive the augmented Lagrange function as

$$\begin{aligned} \mathcal{L}(\mathbf{L}_d,\mathbf{S}_d,\mathbf{S}_{MD},\mathbf{Y}_d,\mathbf{Y}_H)=&\sum_{d=1}^{D}\left(\|\mathbf{L}_d\|_*+\beta_1\operatorname{Tr}\left(\mathbf{L}_d\mathbf{B}\mathbf{L}_d^H\right)+\|\mathbf{S}_d\|_1\right)+\|\mathbf{S}_{MD}\|_1 \\ &+\sum_{d=1}^{D}\left(\langle\mathbf{Y}_d,\mathbf{L}_d-\operatorname{IFFT}(\mathbf{S}_d)\rangle+\frac{\mu_d}{2}\|\mathbf{L}_d-\operatorname{IFFT}(\mathbf{S}_d)\|_F^2\right) \\ &+\langle\mathbf{Y}_E,\mathbf{H}-R_1(\mathbf{L}_1)-R_2(\mathbf{L}_2)-\mathbf{S}_{MD}\rangle \\ &+\frac{\mu_E}{2}\|\mathbf{H}-R_1(\mathbf{L}_1)-R_2(\mathbf{L}_2)-\mathbf{S}_{MD}\|_F^2 \end{aligned} \tag{40}$$

Also, the cost function is decomposed as

$$\begin{cases} \mathbf{L}_d^{(k+1)}=\min\limits_{\mathbf{L}_d}\mathcal{L}\left(\mathbf{L}_1,\mathbf{L}_2,\mathbf{Y}^{(k)}\right) \\ \mathbf{S}_d^{(k+1)}=\min\limits_{\mathbf{S}_d}\mathcal{L}\left(\mathbf{S}_1,\mathbf{S}_2,\mathbf{Y}^{(k)}\right) \\ \mathbf{S}_{MD}^{(k+1)}=\min\limits_{\mathbf{S}_{MD}}\mathcal{L}\left(\mathbf{L}_1,\mathbf{L}_2,\mathbf{Y}^{(k)}\right) \\ \mathbf{Y}_1^{(k+1)}=\mathbf{Y}_1^{(k)}+\mu_1\left(\mathbf{L}_1^{(k)}-\operatorname{IFFT}(\mathbf{S}_1)\right) \\ \mathbf{Y}_2^{(k+1)}=\mathbf{Y}_2^{(k)}+\mu_2\left(\mathbf{L}_2^{(k)}-\operatorname{IFFT}(\mathbf{S}_2)\right) \\ \mathbf{Y}_E^{(k+1)}=\mathbf{Y}_E^{(k)}+\mu_E(\mathbf{H}-R_1(\mathbf{L}_1)-R_2(\mathbf{L}_2)-\mathbf{S}_{MD}) \end{cases} \tag{41}$$

Fixing all the variables except $\mathbf{L}_1$, we derive the augmented Lagrange function of $\mathbf{L}_1$ as

$$\begin{aligned}\mathcal{L}(\mathbf{L}_1) = &\|\mathbf{L}_1\|_* + \beta_1 \mathrm{Tr}\left(\mathbf{L}_1 \mathbf{B} \mathbf{L}_1^H\right) + \langle \mathbf{Y}_1, \mathbf{L}_1 - \mathrm{IFFT}(\mathbf{S}_1)\rangle + \frac{\mu_1}{2}\|\mathbf{L}_1 - \mathrm{IFFT}(\mathbf{S}_1)\|_F^2 \\ &+ \langle \mathbf{Y}_E, \mathbf{H} - R_1(\mathbf{L}_1) - R_2(\mathbf{L}_2) - \mathbf{S}_{MD}\rangle + \frac{\mu_E}{2}\|\mathbf{H} - R_1(\mathbf{L}_1) - R_2(\mathbf{L}_2) - \mathbf{S}_{MD}\|_F^2\end{aligned} \tag{42}$$

The gradient of a part of (42) at $\mathbf{L}_1 = \mathbf{L}_1^{(k)}$ is written as

$$\begin{aligned}\nabla q(\mathbf{L}_1) = &\beta\left(\mathbf{L}_1^{(k)}\mathbf{B} + \mathbf{L}_1^{(k)}\mathbf{B}^T\right) + \mathbf{Y}_1 + \mu_1(\mathbf{L}_1 - \mathrm{IFFT}(\mathbf{S}_1)) \\ &- R_1^*(\mathbf{Y}_3) - \mu_E R_1^*(\mathbf{H} - R_1(\mathbf{L}_1) - R_2(\mathbf{L}_2) - \mathbf{S}_{MD})\end{aligned} \tag{43}$$

Therefore, $\mathbf{L}_1$ is reasonably approximated as

$$\mathbf{L}_1^{(k+1)} = \Re_{1/\eta}\left(\mathbf{L}_1^k - 1/\eta \nabla q(\mathbf{L}_1)\right) \tag{44}$$

Also, the strategy of updating $\mathbf{L}_2$ is similar to $\mathbf{L}_1$. As for updating $\mathbf{S}_1$, $\mathbf{S}_2$, $\mathbf{S}_{MD}$, $\mathbf{Y}_1$, $\mathbf{Y}_2$, and $\mathbf{Y}_E$, the rule is the same as Section 4.2. In summary, we give the overall steps in Algorithm 2. It is noted that we perform 12 multiplications, 22 FFT, and 2 SVD for Algorithm 1. As for Algorithm 2, we perform 16 multiplications, 22 FFT, and 2 SVD in each iteration. Suppose that the size of the HRRP matrix is $\mathrm{N} \times \mathrm{N}$, the computational complexity in a single iteration is about $\mathrm{O}(\mathrm{N}^3 + \mathrm{N}^2 \log \mathrm{N})$. Furthermore, the algorithm typically converges within 70 iterations, which ensures that it does not impose a significant computational burden.

Algorithm 2 Triple-constraint-based accurate separation

Input: Range profiles $\mathbf{H}$, Coarse motion compensation transformation of target1 $R_1(\cdot)$, Coarse motion compensation transformation of target2 $R_2(\cdot)$.
Output: HRRPs of target1 $\mathbf{L}_1$, HRRPs of target2 $\mathbf{L}_2$, HRRPs of micro-motion components $\mathbf{S}_{MD}$, Imaging result of target1 $\mathbf{S}_1$, Imaging result of target2 $\mathbf{S}_2$.
Initialization: $\mathbf{L}_1^{(0)} = \mathbf{L}_2^{(0)} = \mathbf{S}_1^{(0)} = \mathbf{S}_2^{(0)} = \mathbf{S}_1^{(0)} = \mathbf{Y}_E^{(0)} = \mathbf{Y}_1^{(0)} = \mathbf{Y}_2^{(0)} = \mathbf{0}^{N\times M}$, $\mu_1 = \mu_2 = \mu_E = 10^{-4}$, $\beta = 10^{-8}$, $\varepsilon = 1.05$.
while not converged **do**
  The update of the rigid body in the HRRPs domain.
  $\nabla q(\mathbf{L}_1) = \beta\left(\mathbf{L}_1^{(k)}\mathbf{B} + \mathbf{L}_1^{(k)}\mathbf{B}^T\right) + \mathbf{Y}_1 + \mu_1(\mathbf{L}_1 - \mathrm{IFFT}(\mathbf{S}_1))$
    $-R_1^*(\mathbf{Y}_E) - \mu_E R_1^*(\mathbf{H} - R_1(\mathbf{L}_1) - R_2(\mathbf{L}_2) - \mathbf{S}_{MD})$
  $\mathbf{L}_1^{(k+1)} = \Re_{1/\eta}\left(\mathbf{L}_1^k - 1/\eta \nabla q(\mathbf{L}_1)\right)$
  $\nabla q(\mathbf{L}_2) = \beta\left(\mathbf{L}_2^{(k)}\mathbf{B} + \mathbf{L}_2^{(k)}\mathbf{B}^T\right) + \mathbf{Y}_2 + \mu_2(\mathbf{L}_2 - \mathrm{IFFT}(\mathbf{S}_2))$
    $-R_2^*(\mathbf{Y}_E) - \mu_E R_2^*(\mathbf{H} - R_1(\mathbf{L}_1) - R_2(\mathbf{L}_2) - \mathbf{S}_{MD})$
  $\mathbf{L}_2^{(k+1)} = \Re_{1/\eta}\left(\mathbf{L}_2^k - 1/\eta \nabla q(\mathbf{L}_2)\right)$
  The update of the rigid body in the image domain.
  $\nabla q(\mathbf{S}_1) = -\mathrm{FFT}(\mathbf{Y}_1) - \mu_1 \mathrm{FFT}(\mathbf{L}_1 - \mathrm{IFFT}(\mathbf{S}_1))$
  $\mathbf{S}_1^{(k+1)} = \Im_{1/\eta}\left(\mathbf{S}_1^k - 1/\eta \nabla q(\mathbf{S}_1)\right)$
  $\nabla q(\mathbf{S}_2) = -\mathrm{FFT}(\mathbf{Y}_2) - \mu_2 \mathrm{FFT}(\mathbf{L}_2 - \mathrm{IFFT}(\mathbf{S}_2))$
  $\mathbf{S}_2^{(k+1)} = \Im_{1/\eta}\left(\mathbf{S}_2^k - 1/\eta \nabla q(\mathbf{S}_2)\right)$
  The update of the micro-motion components in the HRRPs domain.
  $\nabla q(\mathbf{S}_{MD}) = -\mathbf{Y}_E - \mu_E(\mathbf{H} - R_1(\mathbf{L}_1) - R_2(\mathbf{L}_2) - \mathbf{S}_{MD})$
  $\mathbf{S}_{MD}^{(k+1)} = \Im_{1/\eta}\left(\mathbf{S}_{MD}^k - 1/\eta \nabla q(\mathbf{S}_{MD})\right)$
  The update of the the Lagrange multiplier matrices.
  $\mathbf{Y}_1^{(k+1)} = \mathbf{Y}_1^k + \mu_1(\mathbf{L}_1 - \mathrm{IFFT}(\mathbf{S}_1))$
  $\mathbf{Y}_2^{(k+1)} = \mathbf{Y}_2^k + \mu_1(\mathbf{L}_2 - \mathrm{IFFT}(\mathbf{S}_2))$
  $\mathbf{Y}_E^{(k+1)} = \mathbf{Y}_E^k + \mu_E(\mathbf{H} - R_1(\mathbf{L}_1) - R_2(\mathbf{L}_2) - \mathbf{S}_{MD})$
  $\mu_1 = \varepsilon\mu_1$, $\mu_2 = \varepsilon\mu_2$, $\mu_E = \varepsilon\mu_E$
  $k = k + 1$;
end while

5. Simulated Results and Analysis

In this section, we will validate the effectiveness of our algorithm through simulated experiments. First, we will introduce the simulation model of the radar and the targets. The radar is assumed to transmit LFM signals with a central frequency of $f_0 = 10$ GHz and a bandwidth of $B = 200$ MHz, respectively. The pulse repetition frequency and pulse width are PRF $= 800$ Hz and $\mathrm{T}_0 = 100$ μs, as shown in Table 1, respectively. For the

targets, the scatterer model and antenna model are illustrated in Figure 6. The red scatterers represent the rigid body of the target, while the blue scatterers represent the micro-motion components of the target. Due to the generally small size of the antenna, the rotational radius of the micro-motion components is set as 2 m.

Table 1. System parameters of the simulated radar.

Motion Parameters	Value
Central frequency f_0	10 GHz
Bandwidth B	200 MHz
Pulse repetition frequency PRF	800 Hz
Pulse width T_0	100 μs

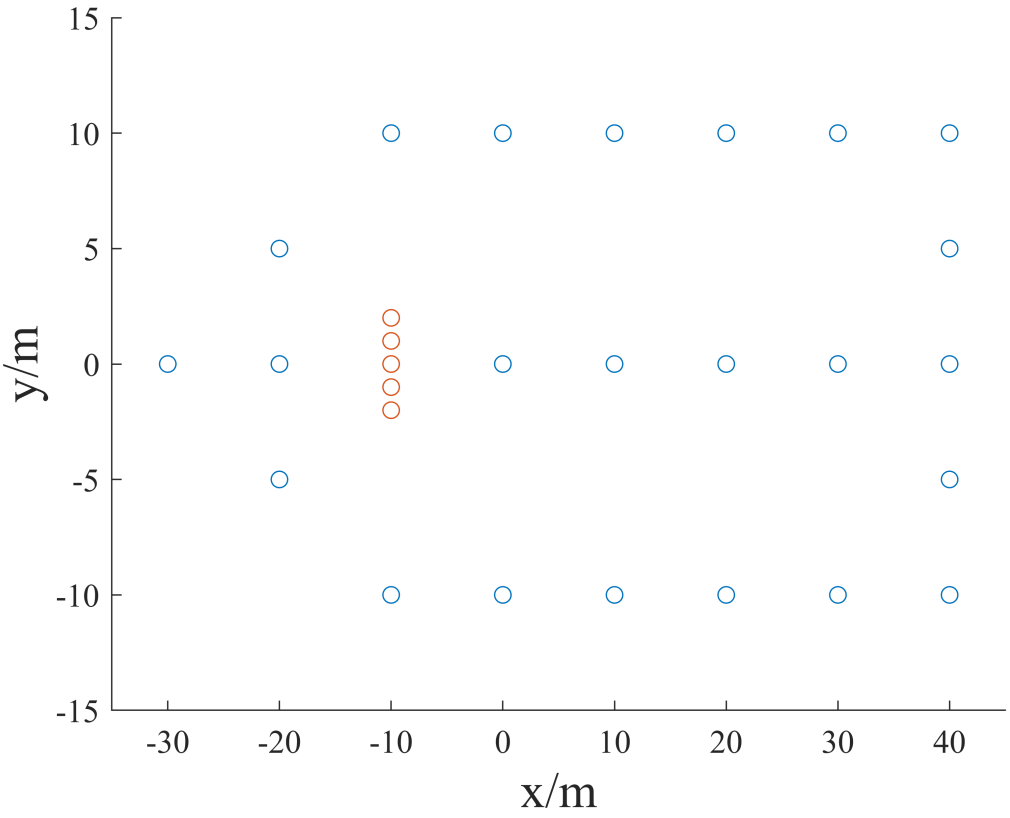

Figure 6. The scatterer model and antenna model of targets.

The motion parameters of the rigid body and the micro-motion components are presented in Table 2. In our assumption, two targets have range overlap along the line of sight (LOS), further causing overlap in the HRRPs domain. Additionally, we add 0 dB complex Gaussian noise to the range profiles without loss of generality.

Figure 7 presents the range profiles with micro-Doppler interference and the multi-target imaging results. It can be seen that under such conditions, the range profiles of different targets severely overlap. Additionally, different targets are connected by interference stripes caused by the micro-Doppler effect in the image domain. As mentioned in Section 4, we first apply a fixed-threshold filter in the image domain to obtain imaging results of the micro-motion components. Then, these imaging results are transformed back into the HRRPs domain to allow the Radon transform to estimate the motion parameters of targets.

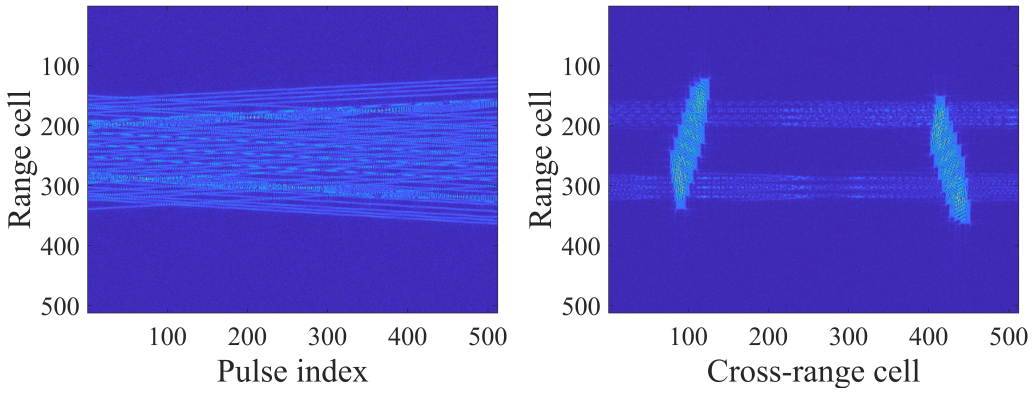

Figure 7. Range profiles and their imaging results. (**a**) Range profiles of targets. (**b**) Imaging result of targets.

Table 2. Motion parameters of rigid body and micro-motion components.

System Parameters	Target1	Target2	Antenna1	Antenna2
X-direction position	3000 m	2900 m	Same as target1	Same as target2
Y-direction position	2000 m	2140 m	Same as target1	Same as target2
X-direction velocity	−7 m/s	8 m/s	Same as target1	Same as target2
Y-direction velocity	0 m/s	0 m/s	Same as target1	Same as target2
Rotational speed	0.02 rad/s	0.02 rad/s	2π rad/s	2.5π rad/s

Figure 8 shows the micro-motion components and their Radon transform results. Figure 8a displays the filtered micro-motion components in the HRRPs domain. Since the translational motion of the micro-motion components is consistent with that of the rigid body, the motion parameters of the rigid body are obtained by estimating the motion parameters of the micro-motion components. The Radon transform is naturally utilized to estimate the motion of different targets. Figure 8b shows the result of applying the Radon transform to Figure 8a. The two peaks circled in red indicate the motion parameters of these two targets. Based on these motion parameters, we generate range migration transformation and input them into the algorithm, as shown in Algorithm 1.

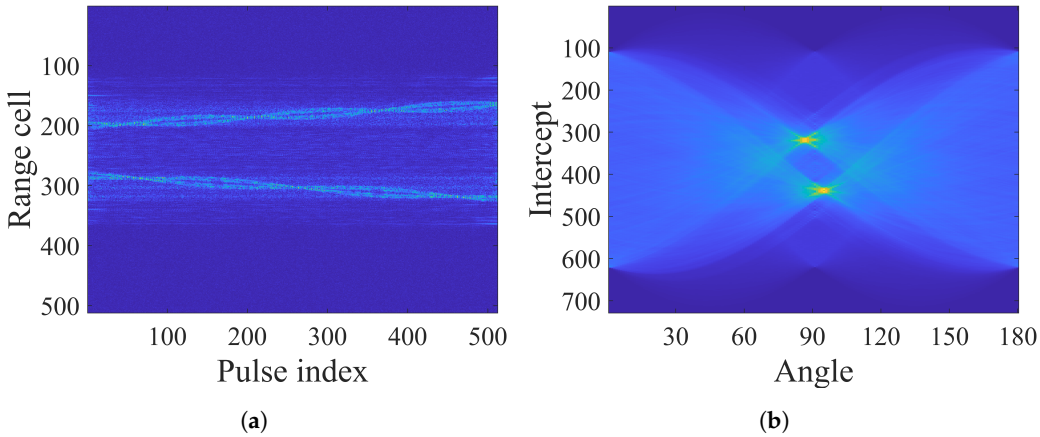

Figure 8. The micro-motion components and their Radon transform results. (**a**) Filtered micro-motion components. (**b**) The Radon transform of the filtered components.

The results of the preliminary separation are presented in Figure 9. Figure 9a,b show the range profiles of different targets, while Figure 9c,d present imaging results of these targets. For clarity, we have magnified several range cells in Figure 9e,f. It can be observed that the range profiles of different targets still exhibit slight range migration, resulting in defocusing in the imaging results. Additionally, signals from the micro-motion components remain in the imaging results. Therefore, further range alignment and target separation are required.

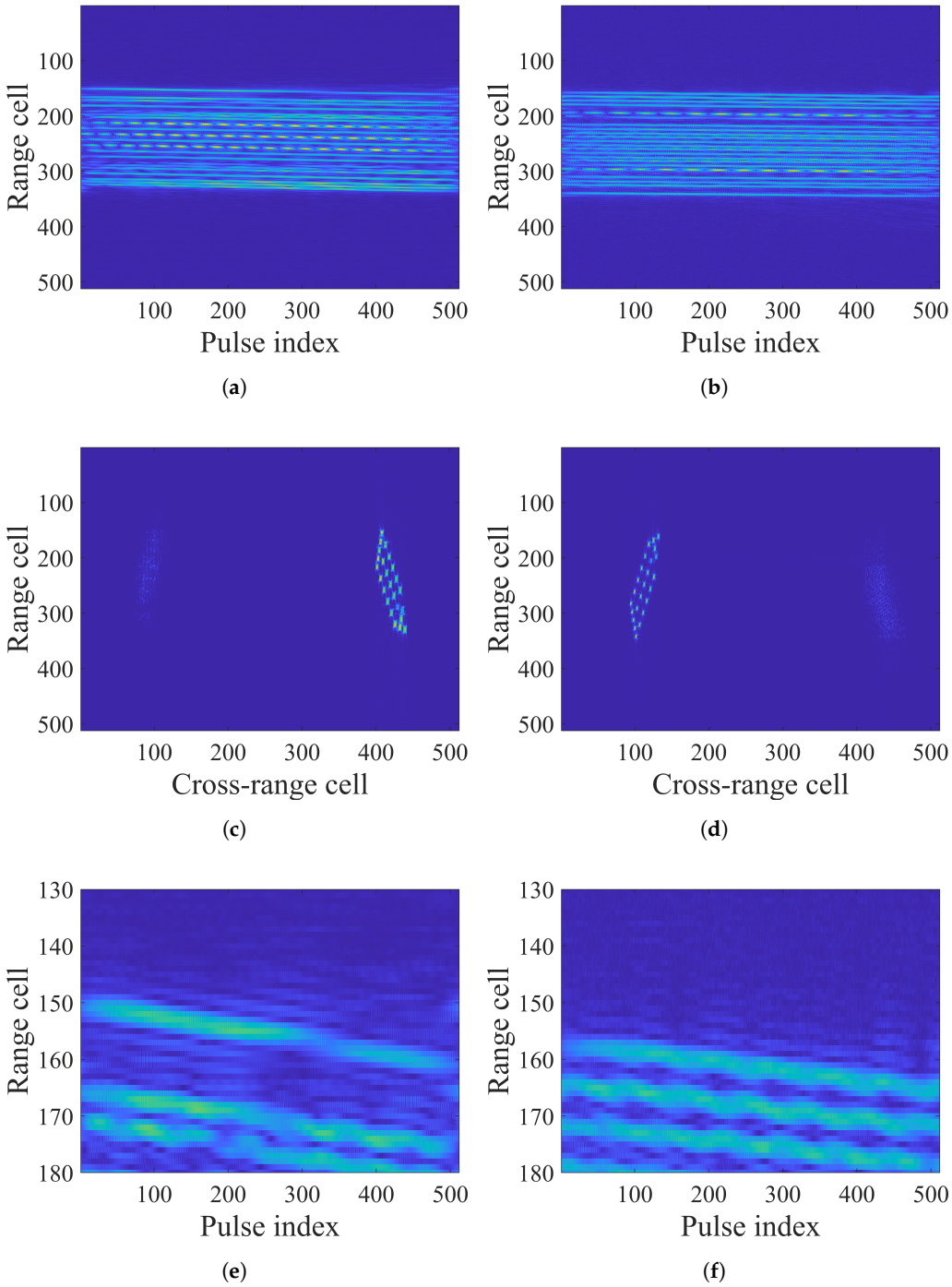

Figure 9. Results of the coarse separation. (**a**) Coarse range profiles of target1. (**b**) Coarse range profiles of target2. (**c**) Coarse imaging result of target1. (**d**) Coarse imaging result of target1. (**e**) Enlarged view of target1. (**f**) Enlarged view of target2.

The MCRA algorithm is used to accurately estimate the range migration of the targets to generate range migration transformation. Figure 10 shows the range profiles of different targets after range alignment and their enlarged views. Figure 10a,d display the range profiles and the enlarged view of target1, while Figure 10b,d display that of target2. Based on these range migration corrections, we completely separate different targets and the micro-Doppler by solving the triple-constraint cost function. The range profiles of different targets and their imaging results are shown in Figure 11. Figure 11a,b display the range profiles and the imaging result of target1, while Figure 11a,b display those of target2. It is clearly visible that different targets are thoroughly separated, and the micro-Doppler interference is suppressed. The image contrast and the image entropy of different stages are given in Table 3. It is seen that our proposed method achieves the entire separation step-by-step.

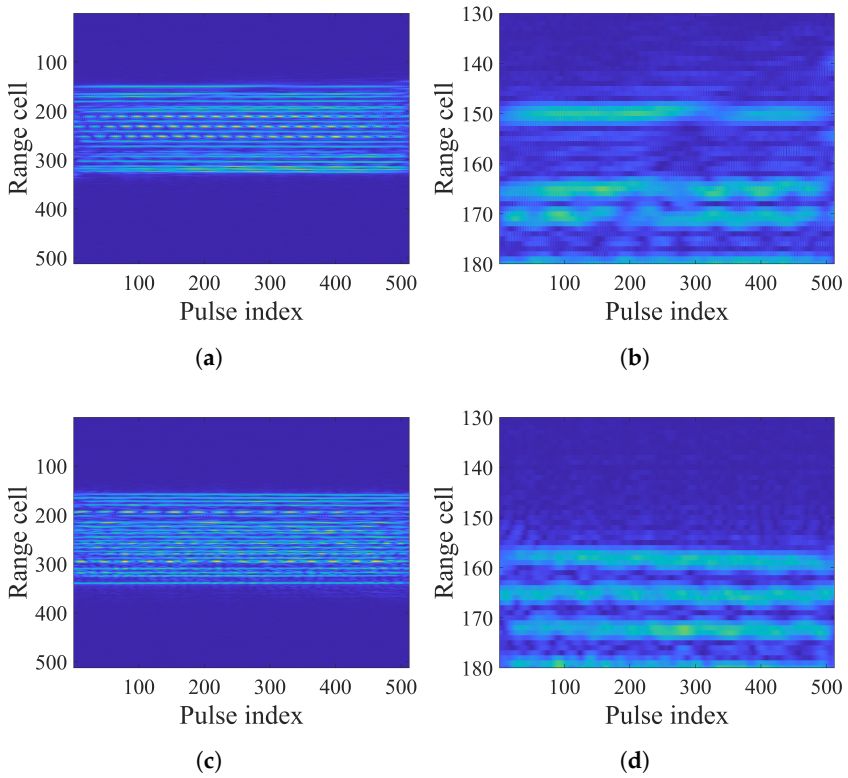

Figure 10. Aligned range profiles and their enlarged views. (**a**) Aligned coarse range profiles of target1. (**b**) Enlarged view of coarse range profiles of target1. (**c**) Aligned coarse range profiles of target1. (**d**) Enlarged view of coarse range profiles of target2.

Table 3. The image contrast and the image entropy in different stages.

Stages	Target Index	Image Contrast	Image Entropy
Original signal	All targets	12.9	4.9
Coarse sepration	Target1	15.8	3.3
	Target2	23.1	9.4
Accurate sepration	Target1	43.4	3.3
	Target2	41.8	9.4

Additionally, we obtain the rotation period of the micro-motion components by performing an auto-correlation transformation, further validating the effectiveness of the separation. Figure 12 shows the aligned micro-motion components in the HRRPs domain and their auto-correlated results. Figure 12a,b indicate the aligned range profiles and the auto-correlated result of target1, while Figure 12c,d show those of target2. It is seen that

the differences of the peaks in Figure 12b,d are about 198 and 159. The pulse repetition interval of the radar is 0.001 s. Therefore, the rotational velocities of these two components are 15.87 rad/s and 19.75 rad/s. The theoretical rotational velocities are about 15.71 rad/s and 18.84 rad/s. The estimated periods are close to the theoretical periods, confirming the effectiveness of our separation procedure.

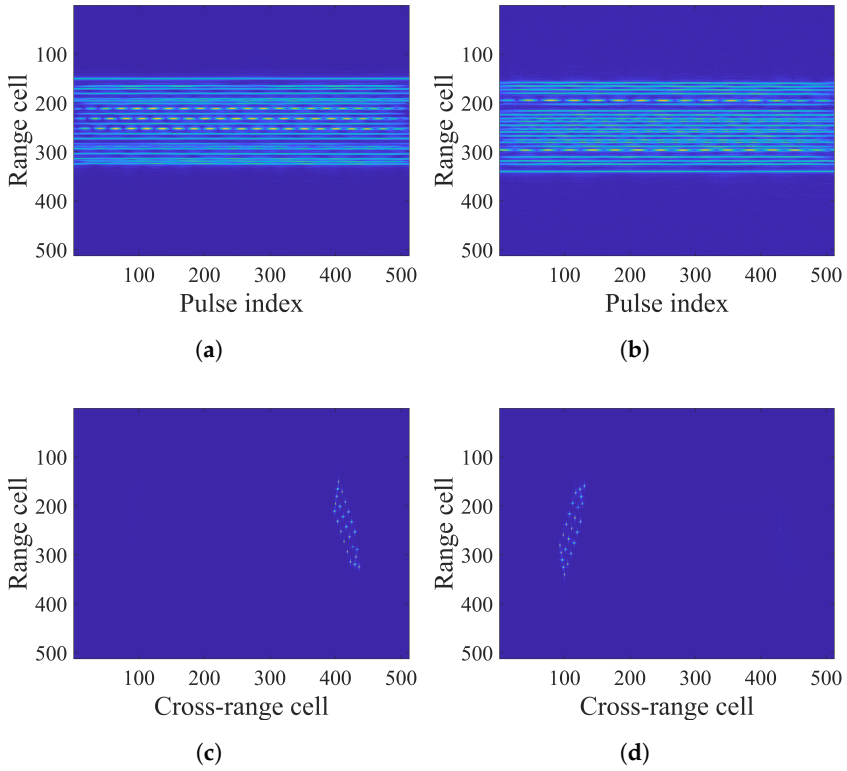

Figure 11. Results of accurate separation. (**a**) Accurate range profiles of target1. (**b**) Accurate range profiles of target2. (**c**) Accurate imaging result of target1. (**d**) Accurate imaging result of target2.

To thoroughly evaluate the effectiveness of the proposed framework, we selected three comparison methods: a TF-based method, a segmentation-based method, and a parameter-based method. Moreover, to further discuss the effectiveness of our algorithm, we analyze scenarios where both the rigid body and the micro-motion components of different targets overlap in the image domain. Figure 13 displays the separation results using these methods, alongside the outcomes of our proposed method. Figure 13a shows the separation result using the TF-based method, which is notably affected by cross-term interference and target overlap, leading to reduced separation performance. Figure 13b presents the separation result from the segmentation-based method, where performance is significantly impacted by the broadening and overlapping of targets in the Doppler domain. Figure 13c demonstrates the parameter-based method's separation results, revealing that interference from different targets lowers the parameter estimation accuracy and thus hampers separation effectiveness. Figure 13d illustrates the separation result using the proposed method, indicating the effectiveness of the proposed method. Furthermore, Table 4 summarizes the separation performance of the different methods. Our proposed method achieves the lowest image entropy and highest image contrast, indicating its superior ability in target separation.

To evaluate the performance of our algorithm under varying signal-to-noise ratios (SNRs), Figure 14 illustrates the separation results at −5 dB, 0 dB, 5 dB, and 10 dB SNR levels. The algorithm achieves satisfactory results within the 0–10 dB range. However, its effectiveness significantly diminishes when the SNR drops below 0 dB.

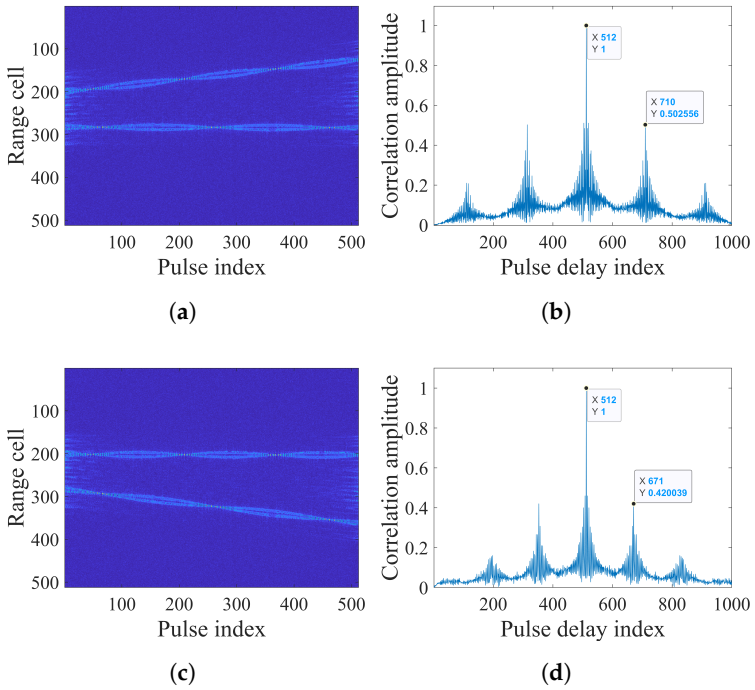

Figure 12. Range profiles of micro-motion components of targets and their auto-correlation results. (**a**) Aligned range profiles of micro-motion components of target1. (**b**) The auto-correlation result of micro-motion components of target1. (**c**) Aligned range profiles of micro-motion components of target2. (**d**) The auto-correlation result of micro-motion components of target2.

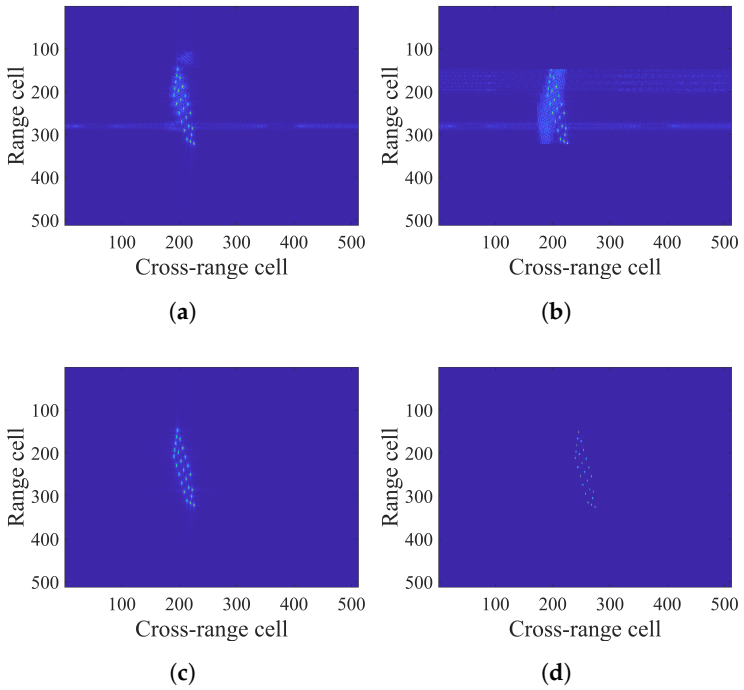

Figure 13. The separation results of different methods and the proposed method. (**a**) The separation result using the TF-based method. (**b**) The separation result using the segmentation-based method. (**c**) The separation result using the parameter-based method. (**d**) The separation result using the proposed method.

Table 4. The image contrast and the image entropy of different methods.

Different Methods	Target Index	Image Contrast	Image Entropy
TF-based method	Target1	21.8	8.2
	Target2	21.5	10.1
Segmentation-based method	Target1	14.8	6.4
	Target2	14.3	9.7
Parameter-based method	Target1	28.1	7.7
	Target2	29.7	10.3
The proposed method	Target1	43.4	3.3
	Target2	41.8	9.4

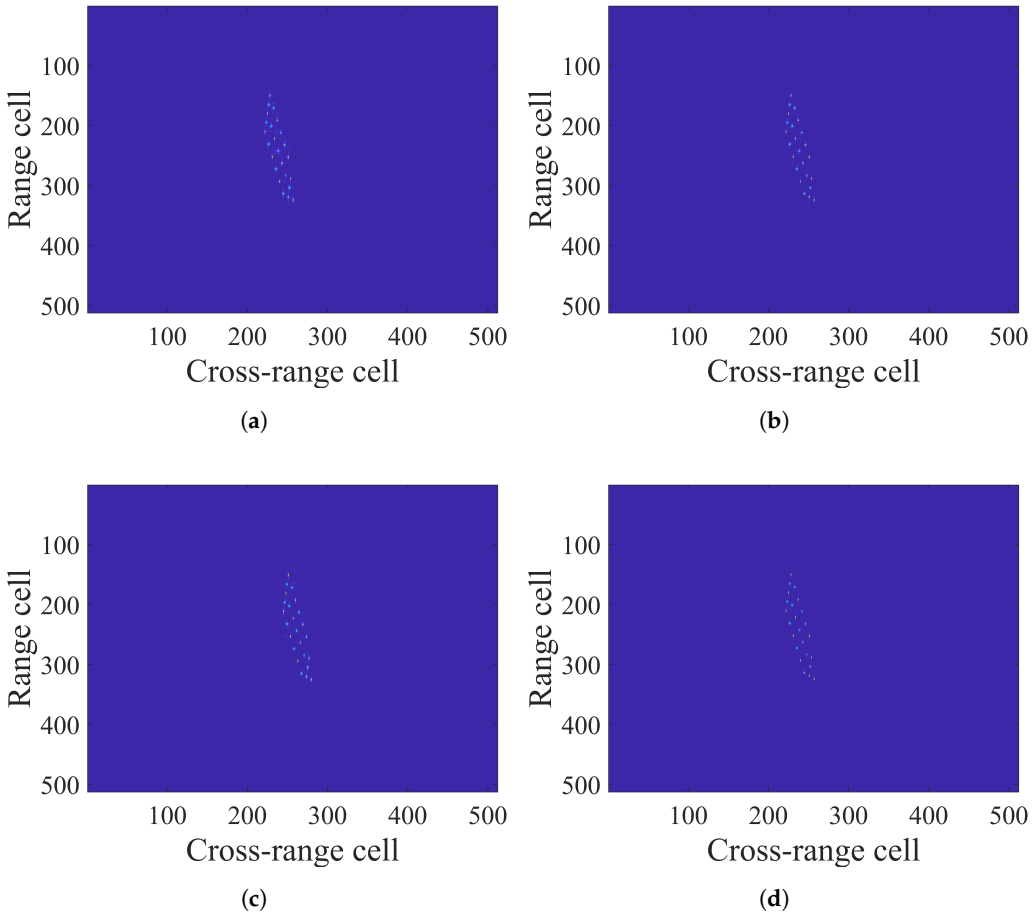

Figure 14. The separation results under different SNR conditions. (**a**) The separation result under the −5 dB SNR condition. (**b**) The separation result under the 0 dB SNR condition. (**c**) The separation result under the 5 dB SNR condition. (**d**) The separation result using the proposed method.

To demonstrate the impact of the initial value of $\mathbf{Y_d}$ on the separation performance, Figure 15 shows the curve related to the separation contrast and the initial value of $\mathbf{Y_d}$. The initial value of the $\mathbf{Y_d}$ matrix varies from 0 to 10. It is seen that the initial value of $\mathbf{Y_d}$ has a minimal influence on the accuracy of the algorithm, demonstrating the robustness of our framework. Additionally, The variation in the value of the cost function is presented in Figure 16, which demonstrates that our algorithm exhibits reasonable convergence.

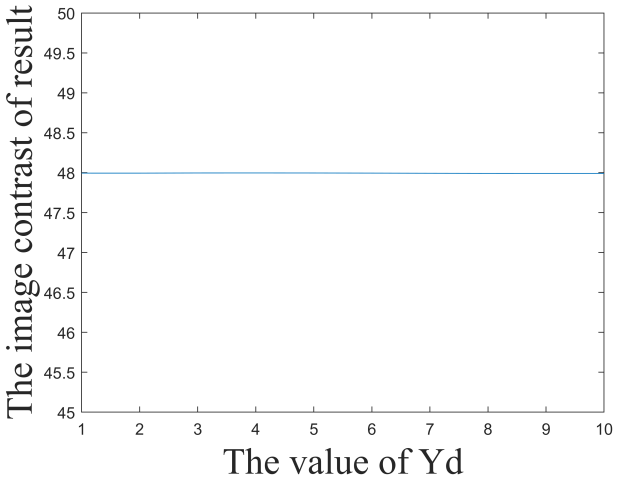

Figure 15. The curve related to the separation contrast and the initial value of $\mathbf{Y_d}$.

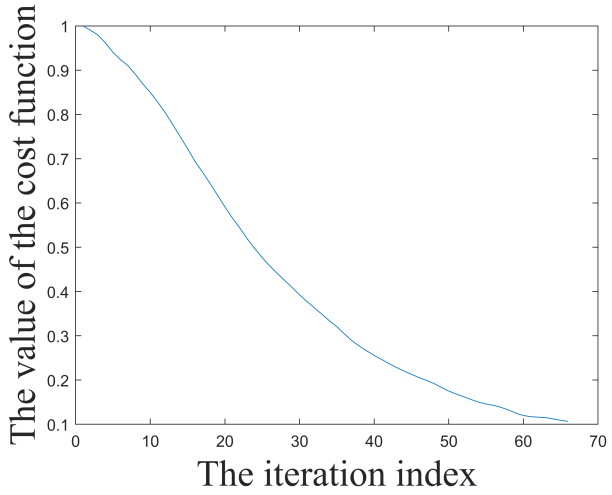

Figure 16. The variation in the value of the cost function.

6. Conclusions

This paper proposes a multi-target ISAR imaging method based on joint constraints with removal of the micro-motion connection. We first estimate the rough translational motion through filtered micro-motion components, reasonably transforming the micro-Doppler interference stripes into the motion information. Following that, we construct the range migration transformation and input this transformation into the double-constraint optimization, thereby roughly separating the targets and the micro-motion components. The separated targets are then utilized to measure the accurate motions and to form the accurate range migration transformation through the MCRA method. Subsequently, the triple-constraints optimization is employed to entirely separate the targets and the micro-motion components. The effectiveness of the proposed method is validated by the simulated experiments.

Author Contributions: Conceptualization, H.L. and F.S.; methodology, H.L.; software, H.L.; validation, H.L.; investigation, H.L.; resources, F.S.; data curation, H.L.; writing—original draft preparation, H.L. and X.L.; writing—review and editing, H.L.; visualization, H.L., X.J., Z.X. and Q.G. All authors have read and agreed to the published version of the manuscript.

Funding: This research received no external funding.

Data Availability Statement: The data presented in this study are available on request from the corresponding author.

Acknowledgments: The authors would like to thank the anonymous reviewers and editors for their valuable comments, which were crucial in improving the quality of this paper.

Conflicts of Interest: The authors declare no conflict of interest.

References

1. Anger, S.; Jirousek, M.; Dill, S.; Peichl, M. Inverse Synthetic Aperture Radar Imaging of Space Targets Using Wideband Pseudo-Noise Signals with Low Peak-to-Average Power Ratio. *Remote Sens.* **2024**, *16*, 1809. [CrossRef]
2. Chen, V.; Martorella, M. *Inverse Synthetic Aperture Radar Imaging: Principles, Algorithms and Applications*; IET : London, UK, 2014.
3. Long, B.; Tang, P.; Wang, F.; Jin, Y.Q. 3-D Reconstruction of Space Target Based on Silhouettes Fused ISAR-Optical Images. *IEEE Trans. Geosci. Remote Sens.* **2024**, *62*, 5213919 . [CrossRef]
4. Gao, Y.; Xing, M.; Li, Y.; Sun, W.; Zhang, Z. Joint translational motion compensation method for ISAR imagery under low SNR condition using dynamic image sharpness metric optimization. *IEEE Trans. Geosci. Remote Sens.* **2021**, *60*, 5108515 . [CrossRef]
5. Wang, J.; Zhang, L.; Du, L.; Yang, D.; Chen, B. Noise-robust motion compensation for aerial maneuvering target ISAR imaging by parametric minimum entropy optimization. *IEEE Trans. Geosci. Remote Sens.* **2019**, *57*, 4202–4217. [CrossRef]
6. Li, Y.; Fu, Y.; Li, X.; Li, L.W. An ISAR imaging method for multiple moving targets based on fractional Fourier transformation. In Proceedings of the 2009 IEEE Radar Conference, Pasadena, CA, USA, 4–8 May 2009; IEEE: Washington, DC, USA, 2009; pp. 1–6.
7. Zhang, D.; Chen, W.; Wang, D. ISAR imaging of multiple moving targets based on RSPWVD-Hough transform. In Proceedings of the 2008 Asia-Pacific Microwave Conference, Hong Kong, China, 16–20 December 2008; IEEE: Washington, DC, USA, 2008; pp. 1–4.
8. Luo, X.; He, Q.; Lv, G.; Shang, C. TSAR imaging of multiple targets based on adaptive Gaussian chirplet decomposition. In Proceedings of the 2006 CIE International Conference on Radar, Shanghai, China, 16–19 October 2006; IEEE: Washington, DC, USA, 2006; pp. 1–4.
9. Fan, L.; Yiming, P.; Shunji, H. Multi-target imaging processing algorithms of ISAR based on time-frequency analysis. In Proceedings of the 2006 CIE International Conference on Radar, Shanghai, China, 16–19 October 2006; IEEE: Washington, DC, USA, 2006; pp. 1–4.
10. Xiao, D.; Su, F.; Wu, J. Multi-target ISAR imaging based on image segmentation and short-time Fourier transform. In Proceedings of the 2012 5th International Congress on Image and Signal Processing, Chongqing, China, 16–18 October 2012; IEEE: Washington, DC, USA, 2012; pp. 1832–1836.
11. Wang, A.; Mao, Y.; Chen, Z. Imaging of multitargets with ISAR based on the time-frequency distribution. In Proceedings of the Proceedings of ICASSP'94. IEEE International Conference on Acoustics, Speech and Signal Processing, Adelaide, SA, Australia, 19–22 April 1994; IEEE: Washington, DC, USA, 1994; p. V-173.
12. Zhang, Y.; Xu, N.; Li, N.; Guo, Z. A Multi-Domain Joint Novel Method for ISAR Imaging of Multi-Ship Targets. *Remote Sens.* **2023**, *15*, 4878. [CrossRef]
13. Chen, J.; Xiao, H.; Fan, H.; Song, Z. ISAR imaging of multiple moving targets using signals separation. In Proceedings of the Proceedings 2013 International Conference on Mechatronic Sciences, Electric Engineering and Computer (MEC), Shenyang, China, 20–22 December 2013; IEEE: Washington, DC, USA, 2013; pp. 1156–1159.
14. Zhao, J.; Zhang, Y.Q.; Wang, X.; Wang, S.; Shang, F. A novel method for ISAR imaging of multiple maneuvering targets. *Prog. Electromagn. Res. M* **2019**, *81*, 43–54. [CrossRef]
15. Bai, X.; Zhou, F.; Xing, M.; Bao, Z. A novel method for imaging of group targets moving in a formation. *IEEE Trans. Geosci. Remote Sens.* **2011**, *50*, 221–231. [CrossRef]
16. Kong, L.; Zhang, W.; Zhang, S.; Zhou, B. Radon transform and the modified envelope correlation method for ISAR imaging of multi-target. In Proceedings of the 2010 IEEE Radar Conference, Arlington, VA, USA, 10–14 May 2010; IEEE: Washington, DC, USA, 2010, pp. 637–641.
17. Xiao, D.; Su, F.; Wu, J. A method of ISAR imaging for multiple targets. In Proceedings of the 2012 IEEE 11th International Conference on Signal Processing, Beijing, China, 21–25 October 2012; IEEE: Washington, DC, USA, 2012; Volume 3, pp. 2011–2015.
18. Jun, S.; Xiaoling, Z.; Shuwei, H. Multi-target ISAR imaging method. In Proceedings of the 2005 IEEE International Geoscience and Remote Sensing Symposium, Seoul, Republic of Korea, 29–29 July 2005; IGARSS'05; IEEE: Washington, DC, USA, 2005; Volume 7, pp. 4745–4748.
19. Chen, J.; Xiao, H.; Song, Z.; Fan, H. Simultaneous ISAR imaging of group targets flying in formation. *Chin. J. Aeronaut.* **2014**, *27*, 1554–1561. [CrossRef]
20. Liu, L.; Zhou, F.; Tao, M.; Zhang, Z. A novel method for multi-targets ISAR imaging based on particle swarm optimization and modified CLEAN technique. *IEEE Sens. J.* **2015**, *16*, 97–108. [CrossRef]
21. Liu, L.; Zhou, F.; Guo, Y.; Tao, M.; Sun, P.; Zhang, Z. A novel method for multi-targets ISAR imaging. In Proceedings of the 2015 IEEE 5th Asia-Pacific Conference on Synthetic Aperture Radar (APSAR), Singapore, 1–4 September 2015 ; IEEE: Singapore , 2015; pp. 314–319.
22. Choi, G.; Park, S.; Kim, H.; Kim, K. ISAR imaging of multiple targets based on particle swarm optimization and hough transform. *J. Electromagn. Waves Appl.* **2009**, *23*, 1825–1834. [CrossRef]

23. Zhao, J.; Zhang, M.; Wang, X.; Nie, D. Parameters estimation and ISAR imaging of multiple maneuvering targets based on an order reduction method for cubic chirps. *J. Electromagn. Waves Appl.* **2017**, *31*, 1658–1675. [CrossRef]
24. Chen, J.; Xiao, H.; Song, Z.; Fan, H. Imaging targets moving in formation using parametric compensation. *EURASIP J. Adv. Signal Process.* **2014**, *2014*, 1–9. [CrossRef]
25. Li, J.; Ling, H. Application of adaptive chirplet representation for ISAR feature extraction from targets with rotating parts. *IEE Proc.-Radar Sonar Navig.* **2003**, *150*, 284–291. [CrossRef]
26. Yuan, B.; Chen, Z.; Xu, S. Micro-Doppler analysis and separation based on complex local mean decomposition for aircraft with fast-rotating parts in ISAR imaging. *IEEE Trans. Geosci. Remote Sens.* **2013**, *52*, 1285–1298. [CrossRef]
27. Lu, L.; Chen, P.; Wu, L. A RPCA-based ISAR imaging method for micromotion targets. *Sensors* **2020**, *20*, 2989. [CrossRef] [PubMed]
28. Zhou, W.; Yeh, C.; Jin, R.; Li, Z.; Song, S.; Yang, J. ISAR imaging of targets with rotating parts based on robust principal component analysis. *IET Radar Sonar Navig.* **2017**, *11*, 563–569. [CrossRef]
29. Zhang, S.; Liu, Y.; Li, X.; Hu, D. Removal of micro-Doppler effect of ISAR image based on Laplacian regularized nonconvex low-rank representation. *IEEE Trans. Image Process.* **2021**, *30*, 6446–6458. [CrossRef] [PubMed]
30. Lin, Z.; Liu, R.; Su, Z. Linearized alternating direction method with adaptive penalty for low-rank representation. *Adv. Neural Inf. Process. Syst.* **2011**, *24* .
31. Cai, J.F.; Candès, E.J.; Shen, Z. A singular value thresholding algorithm for matrix completion. *SIAM J. Optim.* **2010**, *20*, 1956–1982. [CrossRef]
32. Yin, M.; Gao, J.; Lin, Z. Laplacian regularized low-rank representation and its applications. *IEEE Trans. Pattern Anal. Mach. Intell.* **2015**, *38*, 504–517. [CrossRef] [PubMed]